Mehran University Research Journal of Engineering and Technology

https://doi.org/10.22581/muet1982.2955

2024, 43(2) 46-64

# A numerical analysis of mixing and separating of Newtonian fluids in a channel filled with porous materials

Rahim Bux Khokhar [a], Afaque Ahmed Bhutto [b,*], Iftikhar Ahmed Bhutto [c], Fozia Shaikh [a], Kamran Nazeer Memon [d], Prem Kumar [a]

[a] *Department of Basic Science and Related Studies, Mehran University of Engineering and Technology, Jamshoro, Pakistan*

[b] *Department of Basic Science and Related Studies, The University of Larkano, Pakistan*

[c] *Department of Mathematics, Sukkur Institute of Business Administration University, Kandhkot campus Pakistan*

[d] *Department of Mathematics, Quaid-e-Awam University of Engineering, Science and Technology, Nawab shah, Pakistan*

[*] Corresponding author: Afaque Ahmed Bhutto, Email: afaq_bhutto@uolrk.edu.pk

Received: 04 August 2023, Accepted: 28 March 2024, Published: 01 April 2024

KEYWORDS

Fluid Flow
Porous Media
Inertia
Darcy's Number
Taylor-Galerkin
Unidirectional Flows

ABSTRACT

Fluid flow through porous media in intricate geometries has been a fascinating and challenging area of study in applied mathematics and engineering. This area has immense significance in several sectors, such as petroleum, food processing, pharmaceuticals, groundwater flow, and nuclear reactors. This research investigates the behavior of Newtonian fluids in a conduit filled with a permeable medium under combing and separating stream configurations. The finite element method with the Taylor-Galerkin/Pressure-Correction method is applied in the present study. The stream consists of two reversible setups and two unidirectional streams of linear fluids within a channel filled with porous materials, featuring a sudden gap. To obtain steady solutions, a time-dependent numerical approach is employed. The study examines the effect of intensifying inertia, porosity, and variations in flow rates.

## 1. Introduction

Numerical simulations and analysis of fluid stream within a passage filled with non-porous media. Understanding the behavior of fluid flows and the associated pressure variations is essential in various engineering and scientific applications [1][2][3]. The effect of inertia on stream formation, and pressure are of particular interest. The significance of inertia in examining the movement and behavior of fluid within the channel. By varying the Reynolds number, which is a dimensionless factor encoding the proportion of inertial to viscous forces, we can analyze the effect of inertia on the observed stream structures, and variation in the pressure [4][5][6]. The study of flows in channels has great importance due to its widespread applications in various industries such as chemical, biomedical, and mechanical engineering. The behavior of Newtonian fluids in channels is characterized by the presence of unidirectional and reverse flows. Understanding the dynamics of such flows is critical to optimizing fluid transportation processes and reducing energy consumption [5][7][8]. Over the past half-century, the study of smooth fluid movement through intricate channels and pipes containing permeable and non-permeable ingredients has endured a critical and intriguing in the CFD area, particularly in various managing industries [9][7][10]. Due to the intricate stream behavior of non-linear liquids, which exhibit complex rheologic acreages, and the intricacy of the fields implicated, industrial problems become more challenging to tackle. Hence, these complexities stimulate and

challenge mathematicians and scientists. Many scientists [11][12] analysis the behavior of electrically conducting, incompressible, and isothermal Newtonian fluid-flow in unsteady tank drainage was investigated. By employing both perturbation and Adomian decomposition methods, the researchers obtained an analytical solution, finding that the results from both methods agreed. The study provides explicit expressions for key parameters such as velocity field, flow rate, average velocity, and time required for complete drainage, offering valuable insights into the dynamics of fluid drainage in such systems. The study discusses a number of industrial scenarios, however the author focuses mostly on a select few. Within the petroleum industry, there are industries that process crude oil. The authors also address several reactors associated with the previously listed uses [13][14][15]. Numerous investigations have delved into the dynamics of unidirectional and inverse streams of Newtonian fluids within passages [2][16]. Researchers experimentally scrutinized the characteristics of single-dimensional flow of a linear fluid in a rectangular channel, revealing that the flow's velocity profiles conformed well to laminar flow theory [17][18][19]. Further, Afonso [1] delved into the behavior of reverse flows within a horizontal channel, observing the initiation of reverse flow by a small disruption approaching the inlet, which subsequently evolved interested in a enduring vortex. The examination of these streams within intricate areas, including obstructions, corners, and curved surfaces, holds particular interest because of its relevance to real-world applications [20][21]. The influence of porous media on fluid streams is also significant, with profound implications in disciplines for instance geology, environmental engineering, and oil extraction.

The behavior of incompressible laminar fluid streams in complicated fields, by and with no porous media, has been the subject of several recent investigations [5][2][22]. The advancement of state-of-the-art computing systems has facilitated the development of sophisticated numerical algorithms, enabling practical imitations to examine complex fluid dynamics within areas holding permeable materials, a practice widely recognized and endorsed by global institutions [23]. The CFD approach is anticipated to demonstrate distinctive attributes owing to its capability for constraint-based simulations. Significant progress has been made over the last three decades in improving our understanding of numerical doubts and the nature of streams, including unsteady and turbulent behaviors [24]. Mathematical modelling of stream behaviors, such as mixing and separation, was pioneered by Cochrane [25], with subsequent experimental and numerical solutions employing finite difference methods. Baloch [5] and Afonso [26] further explored these phenomena employing finite element and finite volume techniques, respectively. Mingling and split phenomena in rectangular passages and pipes, with or without porous media, exhibit a range of fascinating stream phenomena, including singularities at acute bends and flow transitions. Investigations have also examined optimized values of hydrodynamic forces in convergent-divergent channels, integrating line surfaces at the outer surfaces of obstacles [27][28]. Studies by Cochrane [25], Dharejo [29], Khokhar [6], Afonso [26], and Echendu [2] have collectively observed diverse flow phenomena within the same domain. Baloch [5] explored combining and splitting streams of extremely flexible fluids utilizing a time-dependent finite element technique, employing Taylor-Petrov-Galerkin algorithms due to the fluids' elastic nature [30]. Furthermore, to achieve second-order correctness in incompressibility, Baloch [5] utilized the pressure-correction approach. The Phan-Thien and Tanner (PTT) constitutive model [31] was used in experiments to study Newtonian fluid streams with equal stream rates in arms and viscoelastic streams. Studying various physical parameters and stream situations, shear-thinning behavior was observed as well as the effects of changing the space between plates [32]. The study by Rahman [34][35] examined hydrodynamic forces experienced by two partially heated circular cylinders positioned between grooved channels. According to Afonso [1], the effects of inertia on flow rate can be mitigated by creeping flow or flow with limited inertia. Linear and viscoelastic liquids have been studied in recent numerical simulations [33]. The study focuses on numerical simulations and analysis of fluid streams within passages filled with non-porous media, crucial for understanding fluid behavior in various engineering and scientific applications. By varying the Reynolds number, which indicates the ratio of inertial to viscous forces, the findings analyses the influence of inertia on stream structures and pressure variations. The study aims to examine the influence of inertia on flow patterns and stress in Newtonian fluid streams within conduits containing permeable media. It also seeks to analyse how fluid streams behave under various flow rates and configurations, including both reversed and unidirectional flows.

## 2. Problem Specification

The schematic features of the two flow glitches under consideration, namely (a) repeal stream and (b) unidirectional stream, (c) Reversed stream, and (d) unidirectional stream are shown in Fig. 1[a - d]. Two thin-plate inserts are installed to separate the channel into two portions. The inserts are spaced apart by a gap width β and are aligned horizontally in exactly the center axis line of the geometry. The parting gap β is 3L with L being the characteristic length equal to the height of each input conduit arm. The plates are considered α=0.0254L thick. To simulate a fully developed entrance and exit flow, a conduit with a length of 23L is chosen as being adequately long. The aforementioned criteria have made it possible to compare the numerical predictions directly to experimental data as well as to numerical results from the literature [23][25][1][5].

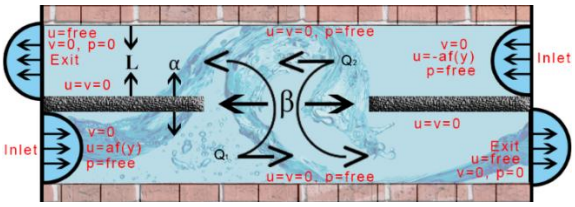


(a) Flow Diagram Showing Two Inlets and Two Exits (Reverse Flow)

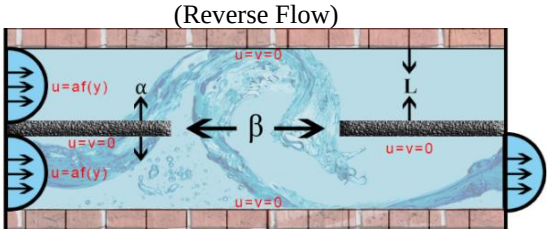


(b) Two Inlets and One Outlet In A Unidirectional Flow

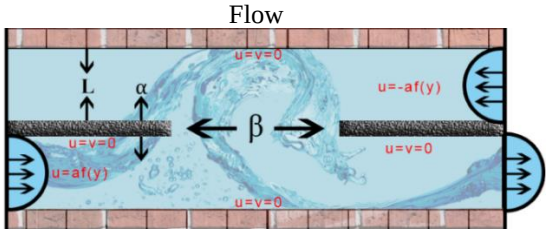


(c) Two Inlets And One Outlet For Opposite Flow $G_3$

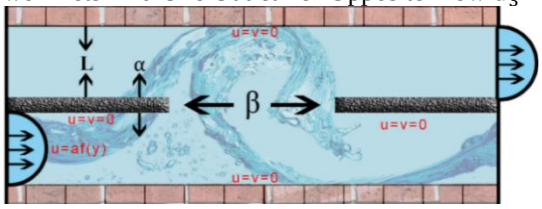


(d) One Inlet and One Outlet In A Unidirectional Flow $G_4$

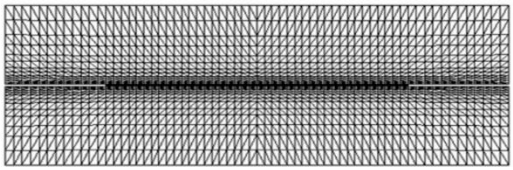

(e) Finite Mesh Element

**Fig. 1.** Geometrical Parameters of The Computational Domain and Mesh

In this study, triangular elements generated by uniform conformal mapping are used to discretize the flow domain. There is a minimum element size of 0.003 times the characteristic length L in the vicinity of the gap region. There are 1328 elements and 2853 nodes in the finite element mesh applied to the domain. The boundaries of these nodes comprise 392 and the vertex nodes comprise 763. For analysis, the mesh provides a total of 6469 degrees of freedom. Reference [21] conducted pioneering work on the selection of time-steps. A time-stepping scheme that is most employed in this study is a procedure that relies on a size of mesh layout determined by the smallest radius of encirclement across the triangular elements. To determine the time step based on the mesh layout, one common approach is to use the Courant-Friedrichs-Lewy (CFL) condition. This condition ensures numerical stability by limiting the time step based on the maximum velocity and the grid spacing in the mesh. The CFL condition is given by:

$$\Delta t \leq \frac{C\Delta x}{u_{max}}$$

Where Δt is the time step, C is a stability factor (typically less than 1), Δx is the grid spacing (mesh size), u_max is the maximum velocity in the domain. The time step is chosen such that it satisfies the CFL condition for stability. This means that the time step is limited by the smallest grid spacing and the maximum velocity in the domain, ensuring that no information travels more than one grid cell per time step.

## 3. Mathematical Formulation

In a conduit with a permeable medium, Newtonian fluid is flowing unsteadily, incompressible, and laminar. It is due to the sudden imposing of a pressure gradient that causes the unsteadiness of the fluid flow. With governing equations based on mass and momentum transport (Darcy-Brinkman) [6], Newtonian fluids can move through a porous material if it is thought to be identical and isotropic. An exact solution was obtained based on the governing equations, aiming to analyze velocity under gravity and hydrostatic force[28]. The second law of motion is applied to the x-component of the transport equation:

$$\sum F_x = \rho a_x \quad (1)$$

Where, $a_x$ defines the acceleration and in x-direction, the force $F_x$ equal to:

$$F_x = \nabla . \sigma + \rho g \nabla h \quad (2)$$

Where $\sigma$ presents Cauchy's stress tensor, the stress tensor is a measure of traction on any surface.

Gravity and height represented by $g, h$. Surface forces are represented by the first term, while second body forces are represented by the second term of Eq. (2).

$$a_x = \frac{Dv}{Dt} = \left(\frac{\partial v}{\partial t} + (v.\nabla)v\right) \quad (3)$$

In Eq. (3), the time is t, $\frac{Dv}{Dt}$ is the material time derivative. The momentum equation is expressed in general vector notation as follows [5]:

$$\rho\left(\frac{\partial v}{\partial t} + (v.\nabla)v\right) = \nabla\sigma + \rho F \quad (4)$$

It is possible to decompose stress tensor into the sum of the following equations for incompressible fluids:

$$\sigma = -p\delta + \underline{\underline{T}} \quad (5)$$

Here, pressure for isotropous fluid is p, $\underline{\underline{T}}$ is extra stress tensor, and $\delta$ represents the components of unit tensor. Newtonian viscous fluids are incompressible, so extra-stress is proportional to strain rate is defined:

$$\underline{\underline{T}} = 2\mu\underline{\underline{D}} \quad (6)$$

In Eq. (6) dynamic viscosity is $\mu$ and rate of deformation tensor $\underline{\underline{D}}$ is defined as [5]:

$$\underline{\underline{D}} = \frac{1}{2}\left(\frac{\partial v_i}{\partial x_j} + \frac{\partial v_j}{\partial x_i}\right) \quad (7)$$

In general notation:

$$\underline{\underline{D}} = \frac{1}{2}[\nabla v + (\nabla v)^{\dagger}] \quad (8)$$

Where, † is transpose of tensor, in extended matrix:

$$\underline{\underline{D}} = \frac{1}{2}\begin{bmatrix} 2\frac{\partial u}{\partial x} & \left(\frac{\partial u}{\partial y} + \frac{\partial v}{\partial x}\right) & \left(\frac{\partial u}{\partial z} + \frac{\partial w}{\partial x}\right) \\ \left(\frac{\partial u}{\partial y} + \frac{\partial v}{\partial x}\right) & 2\frac{\partial v}{\partial y} & \left(\frac{\partial v}{\partial z} + \frac{\partial w}{\partial y}\right) \\ \left(\frac{\partial u}{\partial z} + \frac{\partial w}{\partial x}\right) & \left(\frac{\partial v}{\partial z} + \frac{\partial w}{\partial y}\right) & 2\frac{\partial w}{\partial z} \end{bmatrix} \quad (9)$$

The deformation rate tensor $\underline{\underline{d}}$ depends linearly on the extra stress tensor $\underline{\underline{T}}$ without the use of body force and utilizing the Eq. (4) and (5) into Eq. (6) gives Navier-Stokes equation as follows:

$$\rho\frac{\partial v}{\partial t} = \nabla.\left(2\mu\underline{\underline{d}}\right) - \rho(v.\nabla)v - \nabla p \quad (10)$$

Newtonian fluid $\mu$ assumed to be a constant. Hence, Eq. (10) becomes.

$$\frac{\partial v}{\partial t} = \mu\nabla^2 v - (v.\nabla)v - \nabla p \quad (11)$$

Where,$\nabla$ vector differential operator that is known as a gradient and $\nabla^2$is a Laplacian operator. The characteristic velocity $v_c$, length $L_c$ and the time scale of $\frac{L_c}{v_c}$. are chosen to raise the non-dimensionalities. The governing equations are effectively transformed into a non-dimensional form. The dimensionless elements $x^*, v^*, p^*$ and $t^*$ are specified by the inclusion of appropriate scales denoted as:

$$x = L_c x^*, \quad v = v_c v^*, \quad p = \rho {v_c}^2 p^*, \text{ and } \quad t = \frac{L_c}{v_c}t^*$$

For concern of simplicity and devoid of vagueness all identify notations might be abandoned and Eq. (12) could be identified non-dimensionally as [5] :

$$\frac{\partial v}{\partial t} = \frac{1}{Re}\nabla^2 v - (v.\nabla)v - \nabla p \quad (12)$$

Where, $Re$ is a Reynolds number and extracted as:

$$Re = \frac{\rho v_c L_c}{\mu} \quad (13)$$

*3.1 Initial and Boundary Conditions*

To accomplish the problem requirement, it is needed to set initial and boundary conditions. Eq. (12) is extended by boundary condition specified as:

$$v(x, 0) = v_0(x) \quad (14)$$

Subject to

$$\nabla \cdot v_0 = 0 \quad (15)$$

A no-slip condition is applied to the monochrome walls of the geometry, as well as the plates embedded at the center, in which all components of the velocity field become zero. As described in Eq. (16) and (17), a steady Poiseuille stream profile is enforced at both inlet and outlet sectors of the conduit in both sections. Different boundary conditions are applied when different flow rates or directions are encountered. In order to simplify the process, a pure estimate is employed, which has been shown not to compromise solution accuracy and makes frequent entry into flow regions possible. The transient simulation of constant inertia begins from stationary conditions and finds a steady-state result. Earlier steady-state solutions are used as the initial terms for higher variable values to expedite calculation times. This relates to objects at together inlets:

$$u(y) = U_m(y-a)(b-y) \; at \; x = 0 \quad \text{(Lowest left arm)} \quad (16)$$

$$u(y) = -V_m\{y - (b + \alpha)\}(2b + \alpha - y) \; at \; x = 23L \quad \text{(Top right arm)} \quad (17)$$

The wall of the numerical domain has a height of $b - a$, and its bottom and upper coordinates are defined by Eq. (16) and Eq. (17), with $\alpha = 0.0254$ denoting the plate's thickness. With a fair length of $23L$, the canal guarantees flow at both inlets and exits. L in this case denotes the channel's precise

length. The bottom left arm, with $a = 0$ and $b = 1$, was affected by the flow at the entrance. The extreme velocity attained in the channel arm center for equal flow rates is represented by $U_m = V_m$, whereas the values for uneven flow rates are represented by $U_m$ and $V_m$, which stand for 1:1.5 and 1:2, respectively.

To make certain consistency with the static pressure $p = 0$, normal traction-free conditions are maintained at the outlet of both geometries. The stream fields are approached numerically, with careful monitoring of the flow regions to ensure that they do not adversely affect the global accuracy of the solutions. The top of the form $v = 0$ assumes no crossover flow at both entrances and exits.

*3.2 Governing Equations for Porous Medium*

Let the case of a two-dimensional Euclidean space bounded by a spatial domain, which can be denoted as $\rightarrow R2$. In this domain, the boundary is piecewise smooth. There is also a time domain [0, I], where $x$ indicates the spatial coordinate and t indicates the time coordinate. To describe the flow behavior of incompressible, isothermal, and isotropic fluid across homogeneous porous media without body forces, we can use the mass conservation, and Darcy-Brinkman momentum transport equations. Both channels and pipes can be modeled using these equations. Flow behavior can be described by the following equation:

$$\rho \frac{\partial v}{\partial t} = \nabla.\left(2\mu \underline{\underline{d}}\right) - \rho(v.\nabla)v - \nabla p - \frac{\omega\mu}{\kappa} v \qquad (18)$$

According to the given equations, the variables represent the following quantities:

$v(x,t)$ represents the vector field at time t in the spatial domain $\Omega$. The isotropic pressure per unit density is represented by $p(x,t)$ in spatial domain $\Omega$ at a given time. $\mu$ and $\rho$ indicate viscosity, and density of the fluid, correspondingly. $\kappa$ refers to permeability of porous media within the domain. The porosity of the porous media in the domain is described by $\Omega$. Assuming that the flow is hydro dynamically fully developed, and the transverse and radial orientations of the conduit or pipe have no impact on the velocity. Utilizing the incompressibility, the flow can be articulated by means of a transverse direction function and an expression for axial velocity. It is possible to derive Eq. (19) using Eq. (12) and Eq. (18) with the view to acquire the dimensionless manner of the equation.

$$\frac{\partial v}{\partial t} = \frac{1}{Re}\nabla^2 v - (v.\nabla)v - \nabla p - \frac{1}{ReD_a} v \qquad (19)$$

Here, $D_a = \frac{\kappa\rho v_c}{\omega\mu L_c}$ denotes the Darcy's non-dimensional number.

The results of this study demonstrate that the fully developed flow is independent of the axial direction of the pipe or channel in terms of hydrodynamic velocity. There is a unidirectional flow indicated by the continuity equation, and its behavior is only reflected by its axial velocity expression. According to the steady-state solutions obtained in this study, porous media exhibit a velocity profile as follows:

$$u(y) = U_{max}\left[1 - \frac{cosh\frac{y-a}{\sqrt{D_a}} + sinh\frac{b-y}{\sqrt{D_a}}}{sinh\frac{b-a}{\sqrt{D_a}}}\right] \qquad (20)$$

In Eq. (20) at bottom inlet at $x = 0$, $U_{max} = U_m$, for $a = 0$, and $b = 1$. However, at top right inlet $x = 23L$, $U_{max} = V_m$ and here $a = 1.0254$ and $b = 2.0254$.

*3.3 Taylor–Galerkin/Pressure–Correction Scheme*

This scheme is a numerical method for resolution partial differential equations (PDEs), intensely those arising in fluid dynamics. In this method, the solution is expressed as a series expansion based on basis functions. Choosing these basis functions such that they approximate the governing equations is the key to success. This method was developed by the mathematicians George I. Taylor and Boris Galerkin [34]. The main goal of the Taylor-Galerkin scheme is to develop a time-stepping approach that is efficient and highly accurate in portraying both transient and steady-state solutions to fluid stream problems. The algorithm was originally obtained by Donea [34] to address time-dependent streams of Newtonian fluids while implicitly addressing the issue of incompressibility. It is possible to discretize time within the procedure by utilizing Taylor series expansions. To ensure second-order temporal accuracy, a two-step predictor-corrector scheme is implemented, integrating the Lax-Wendroff approximation. The algorithm also achieves higher-order correctness for time derivatives and dependable spatial derivatives, providing notable improvements in accuracy and stability over Euler-Galerkin and Finite Difference methods [34][30]. Computational Fluid Dynamics (CFD) simulations commonly use pressure-correction schemes to solve Navier-Stokes equations. Two steps are involved in the process: the Predictor Step and the Corrector Step. Originally proposed by Chorin [35] and later modified by Fortin [13], the Pressure-correction/projection method segregates the pressure and velocity fields and uses linearized momentum analysis to achieve generally second-order accuracy and stability. Several related techniques have been developed using this method, including the TGPC algorithm [36] [37], which has

been applied to this research. In finite difference research, similar approaches can also be observed [5] [38] [39]. Experimental and numerical studies have been conducted on the algorithm in terms of non-Newtonian fluids, both on a semi-implicit and fully implicit basis. The semi-implicit algorithm provides numerical accuracy as well as computational efficiency for flows dominated by diffusion, making it a viable option for a variety of problems. This study employs a semi-implicit variant of the TGCP algorithm, as demonstrated in this paper.

*3.4 Semi–Implicit Time–Stepping Scheme*

A semi-implicit time-stepping method is a numerical approach operated to solve partial differential equations (PDEs) that contain rigid and non- rigid terms. Using three Jacobi mass-matrix iterations, this method aims to obtain an exact result. When implementing a semi-implicit method for Newtonian problems, typical time steps are $\Delta t \leq 0.1$. According to references [40][41], steady state solutions should be achieved by allowing a relative increment tolerance of $10^{-1}$ times the time step.

*3.4.1 Cartesian co-ordinates*

An analysis of the literature indicates that explicit schemes in numerical simulations can be costly because their gradual convergence rate makes managing large time steps difficult. The present research uses a semi-implicit version of the TGCP algorithm directly to its strength and ability to recover correctness, stability, efficiency, and convergence rate at higher time steps [5][30][42]. Although fully implicit algorithms are frequently more expensive, they may not necessarily lead to improved numerical stability. To achieve a balance between accuracy, stability, and computational efficiency, the Crank-Nicolson treatment is selectively applied only to the viscous and diffusive modules and Darcy's modules in this study. It is proposed in [6] to use a semi-implicit methodology for solving the TGCP. It is possible to extend the temporal domain $(t_n, t_{n+1})$ into a bifurcated method by using Taylor series expansion. Using the primitive variables $(v^n, p^n)$ at $t = t_n$, an initial forward difference scheme is implemented to calculate the velocity vector field at transitional time step $\left(n + \frac{1}{2}\right)$. Permitting to [43], this methodology adheres to the finite element concept. The central difference method is employed to verify the primitive variables $(v^{n+1}, p^{n+1})$ at the concluded time step $(t = t_{n+1})$. The Crank-Nicolson technique is managed to address the incompressibility constraint associated with the pressure term, which results in two additional steps. Utilizing the data obtained from the initial step, the second step involves determining a velocity vector field that is non-divergent. In the third stage, a pressure differential must be obtained at the full-time step $(t = t_{n+1})$. The fourth step involves calculating a divergence-free velocity vector field $(v^{n+1})$ using the pressure difference information gathered in the third step. Here is the algorithm for integrating the temporal difference into the semi-discrete Darcy-Brinkman equation:

Stage–1a: Determine a velocity field that is free from divergence $v^{n+\frac{1}{2}}$ at partial time step $n + \frac{1}{2}$ from the Provided the preliminary information for the velocity vector field.$v^n$and pressure$p^n$ at initial level $n$:

$$\left(\frac{2}{\Delta t} - \frac{1}{2Re}\nabla^2 + \frac{1}{2ReD_a}\right)\left(v^{n+\frac{1}{2}} - v^n\right) = \left[\frac{1}{\mathrm{Re}}\nabla^2 v - (v.\nabla)v - \nabla p - \frac{1}{\mathrm{Re\ D}_a}v\right]^n \quad (21)$$

Stage-1b: Determine the middle non–solenoidal speed field $v^*$ velocity vector fields $v^{n+\frac{1}{2}}$ calculated at pressure $p^n$, and time step $n + \frac{1}{2}$ at distinguish time step $n$ when employing Crank–Nicolson conduct on pressure:

$$\left(\frac{1}{\Delta t} - \frac{1}{2\mathrm{Re}}\nabla^2 + \frac{1}{\mathrm{Re\ D}_a}\right)(v^* - v^n) = \left[\frac{1}{\mathrm{Re}}\nabla^2 v - \nabla p - \frac{1}{\mathrm{Re\ D}_a}v\right]^n - (v.\nabla)v^{n+\frac{1}{2}} \quad (22)$$

Stage–2: To determine the pressure variation $(p^{n+1} - p^n)$ at the entire time step interval $(t_n, t_{n+1})$, it is necessary to resolve the non-divergence free velocity vector $v^*$ by using the Poisson equation.

$$\theta\nabla^2(p^{n+1} - p^n) = \frac{1}{\Delta t}\nabla.v^* \quad (23)$$

Stage–3: The methodology for computing the solenoidal rate field $v^{n+1}$ at the end of a single time step $(n + 1)$ is presented in this work in its third and final step. This procedure makes use of data from phases (1b and 2), as well as the intermediate velocity field $v^*$ and pressure difference $(p^{n+1} - p^n)$. This step is determined by the equation that follows:

$$\frac{2}{\Delta t}(v^{n+1} - v^*) = -\nabla(p^{n+1} - p^n) \quad (24)$$

In this equation, a time step index is denoted by. Crank-Nicolson time discretization $(\theta = 0.5)$ is used for this analysis as suggested in previous studies [5][44][42]. The first temporal fractional stage is enhanced by adding a midpoint. The inclusion of this factor facilitates the transition from a first-order

projection scheme to a second-order projection scheme, improving the final solution's accuracy.

3.4.2 *Cylindrical polar co–ordinates*

Several factors determine which algorithm is best for numerical simulation, including accuracy, convergence rate, efficiency, and stability. Several studies demonstrate that semi-implicit methodologies achieve better convergence rates than explicit methodologies [5] [40] [42] [45]. The use of implicit techniques enhances numerical stability without requiring excessive computational resources. Here are the details of Darcy's discrete semi-implicit equations:

Stage–1(a):

$$\left[\frac{2}{\Delta t}M+\frac{1}{Re}\left(\frac{S_{rr}}{2}+\frac{M}{D_a}\right)\right]\left(V_{r,j}^{n+\frac{1}{2}}-V_{r,j}^{n}\right)=\left[-\frac{1}{Re}\{S_{rr}+S_{rz}\}V_{r,j}-J_1^{\dagger}P_k\right]^{n}-N(V)V_{r,j}^{n}-\frac{1}{ReD_a}MV_{r,j}^{n} \quad (25)$$

$$\left[\frac{2}{\Delta t}M+\frac{1}{Re}\left(\frac{S_{zz}}{2}+\frac{M}{D_a}\right)\right]\left(V_{z,j}^{n+\frac{1}{2}}-V_{z,j}^{n}\right)=\left[-\frac{1}{Re}\{S_{rz}^{\dagger}+S_{zz}\}V_{z,j}-J_2^{\dagger}P_k\right]^{n}-N(V)V_{z,j}^{n}-\frac{1}{ReD_a}MV_{z,j}^{n} \quad (26)$$

Stage–1(b):

$$\left[\frac{1}{\Delta t}M+\frac{1}{Re}\left(\frac{S_{rr}}{2}+\frac{M}{D_a}\right)\right]\left(V_{r,j}^{*}-V_{r,j}^{n}\right)=\left[-\frac{1}{Re}\{S_{rr}+S_{rz}\}V_{r,j}-J_1^{\dagger}P_k^{n}\right]^{n}-N(V)V_{r,j}^{n+\frac{1}{2}}-\frac{1}{ReD_a}MV_{r,j}^{n} \quad (27)$$

$$\left[\frac{1}{\Delta t}M+\frac{1}{Re}\left(\frac{S_{zz}}{2}+\frac{M}{D_a}\right)\right]\left(V_{z,j}^{*}-V_{z,j}^{n}\right)=\left[-\frac{1}{Re}\{S_{rz}^{\dagger}+S_{zz}\}V_{z,j}-J_2^{\dagger}P_k^{n}\right]^{n}-N(V)V_{z,j}^{n+\frac{1}{2}}-\frac{1}{ReD_a}MV_{z,j}^{n} \quad (28)$$

Stage–2:

$$K(Q^{n+1})=-\frac{2}{\Delta t}\left(J_1V_{r,j}+J_2V_{z,j}\right) \quad (29)$$

Stage–3:

$$M\left({V_{r,j}}^{n+1}-{V_{r,j}}^{*}\right)=\frac{\Delta t}{2}{J_1}^{\dagger}(p^{n+1}-p^{n}) \quad (30)$$

$$M\left({V_{z,j}}^{n+1}-{V_{z,j}}^{*}\right)=\frac{\Delta t}{2}{J_2}^{\dagger}(p^{n+1}-p^{n}) \quad (31)$$

$S=\int\left\{\frac{\partial\phi_i}{\partial x}\frac{\partial\phi_j}{\partial x}+\frac{\partial\phi_i}{\partial y}\frac{\partial\phi_j}{\partial y}\right\}d\Omega$ is a momentum diffusion matrix, $J_1=\int\frac{\partial\psi_i}{\partial x}\phi_j\,d\Omega$ and $J_2=\int\frac{\partial\psi_i}{\partial y}\phi_j\,d\Omega$ are divergence/pressure gradient matrix and $J=(J_1,J_2)$ and $K=\int\left\{\frac{\partial\psi_{ki}}{\partial x}\frac{\partial\psi_{kj}}{\partial x}+\frac{\partial\psi_{ki}}{\partial y}\frac{\partial\psi_{kj}}{\partial y}\right\}d\Omega$ is a stiffness matrix for pressure, where † is matrix transpose. $V^n, V^*, V^{n+1}$ are nodal vectors of velocity field, the pressure $p^n, p^{n+1}$ , and the time interval $\Delta t$ is $(t_n, t_{n+1})$. $V_j^n$, is a nodal velocity vector at $t_n$ time, $V_j^*$ is an intermediate non-divergence-free velocity vector and $V_j^{n+1}$is a divergence-free velocity vector at time step$t_{n+1}$. In equations, pressure vector is $p_k^n$, and $Q^{n+1}=p_k^{n+1}-p_k^n$ is a pressure difference vector.

*3.5 Finite Element Discretization*

A variational formulation consuming a weighted approach along with a finite element approximation is used to discretize the set of Eq. (21) to Eq. (24) in the spatial domain. The objective of this approach is to represent the equations in a form that allows for numerical approximation. The shape and weight functions are defined in Hilbert spaces that are subsets of the two-dimensional Euclidean space $\Omega\subset\Re^2$. Specifically, we consider the Hilbert space $H^1(\Omega)^2$for scalar-valued functions and their first-order derivatives, and the vector-valued Sobolev space for functions which are integrable squares in the $L^2(\Omega)$ norm with their second-order derivatives. Finite element approximation is based on these function spaces. To obtain an inclusive interpretation of the precise definitions of these function spaces, the interested reader should refer to references [3] and [31]. The approach outlined above represents a standard methodology for discretizing and approximating the equations in question.

$$V=\left\{u^n\subset H^1(\Omega)^2\,\middle|\,u\Gamma_1^{\,n}=b\right\} \quad (32)$$

$$V_0=\{v\subset H^1(\Omega)^2|u\Gamma_1=0\} \quad (33)$$

For integrable square functions, the traditional inner–product exemplification is described as:

$$\langle f,g\rangle=\int_\Omega f(x)\,g(x)d\Omega \quad (34)$$

Given$L^2(\Omega)$ a scalar Hilbert space for square-integrable functions, we can express the following:

$$P=\{q\subset L^2(\Omega)^d\} \quad (35)$$

The following set of Eq. (21) to Eq. (24) implies a weak formulation of the problem. The following semi-discrete variational forms are predicted at different stages:

Stage–1a:

$$\left(\left(\frac{2}{\Delta t}-\frac{1}{2Re}\nabla^2+\frac{1}{2\mathrm{Re}\,\mathrm{D}_a}\right)\left(v^{n+\frac{1}{2}}-v^{n},v\right)\right)=\left(\frac{1}{\mathrm{Re}}\nabla^2v-(v.\nabla)v-\frac{1}{\mathrm{Re}\,\mathrm{D}_a}v,v\right)-(\nabla p,q) \quad (36)$$

Stage–1b:

$$\left(\frac{1}{\Delta t}-\frac{1}{2\mathrm{Re}}\nabla^2+\frac{1}{\mathrm{Re}\,D_a}\right)(v^*-v^n,v)=\left(\frac{1}{\mathrm{Re}}\nabla^2 v-\frac{1}{\mathrm{Re}\,D_a}v,v\right)^n-(\nabla p,q)^n-\left(v.\nabla v^{n+\frac{1}{2}},v\right) \quad (37)$$

Stage–2: $\theta\nabla^2(p^{n+1}-p^n,q)=\frac{1}{\Delta t}(\nabla.v^*,v)$ (38)

Stage–3:

$$\frac{2}{\Delta t}(v^{n+1}-v^*,v)=-\nabla(p^{n+1}-p^n,q) \quad (39)$$

By using weighted residual technique, the above Eq. (35) is spatially discretized using the Galerkin approximation method, in which the weight function is reserved to be equivalent to the shape function. The shape functions consumed for determining velocity and pressure components are piecewise quadratics and piecewise linear over triangular mesh tessellations, respectively. We introduce the approximate solutions of primitive variables, $u(x,y,t), v(x,y,t)\ and\ p(x,y,t)$, over finite spaces of the following functions:

$$u(x,y,t)\cong\sum_{j=1}^{6}U_j^n(t)\,\Phi_j(x,y) \quad (40)$$

$$v(x,y,t)\cong\sum_{j=1}^{6}V_j^n(t)\,\Phi_j(x,y) \quad (41)$$

$$p(r,z,t)\cong\sum_{k=1}^{3}P_k(t)\psi_k(r,z) \quad (42)$$

here, $\psi_k$ and $\Phi_j$ are linear and quadratic shape functions respectively. Eq. (36) to Eq. (39) ssymbolizations are followed [6]. The compact matrix form of the fully discrete system is:

Stage–la:

$$\left[\left\{\frac{2M}{\Delta t}-\frac{1}{Re}\left(\frac{S}{2}+\frac{M}{D_a}\right)\right\}\left(V^{n+\frac{1}{2}}-V^n\right)=\left[-\frac{1}{Re}(SV_j)+j_1^{\dagger}P_k-N(V)V_j-\frac{1}{Re\,D_a}MV_j\right]\right]^n \quad (43)$$

Stage–lb:

$$\left[\frac{M}{\Delta t}-\frac{1}{Re}\left(\frac{S}{2}+\frac{M}{D_a}\right)\right](V^*-V^n)=\left[-\frac{1}{Re}(SV_j)+j_2^{\dagger}P_k-\frac{1}{Re\,D_a}MV_j\right]^n-N(V)V_j^{n+\frac{1}{2}} \quad (44)$$

Stage–2:

$$K(p^{n+1}-p^n)=-\frac{2}{\Delta t}JV_j^* \quad (45)$$

Stage–3:

$$\frac{2M}{\Delta t}\left(V_j^{n+1}-V_j^*\right)=J^{\dagger}(p^{n+1}-p^n) \quad (46)$$

Where $M=\int\phi_i\phi_j d\Omega$ is a consistent mass matrix,

$N(V)=\int\left\{\varphi_i(\phi_l U_l)\frac{\partial\phi_j}{\partial x}+\varphi_i(\phi_l V_l)\frac{\partial\phi_j}{\partial y}\right\}d\Omega$ is a convection matrix,

$S=\int\left\{\frac{\partial\phi_i}{\partial x}\frac{\partial\phi_j}{\partial x}+\frac{\partial\phi_i}{\partial y}\frac{\partial\phi_j}{\partial y}\right\}d\Omega$ is a momentum diffusion matrix, $J_1=\int\frac{\partial\psi_i}{\partial x}\phi_j\,d\Omega$ and $J_2=\int\frac{\partial\psi_i}{\partial y}\phi_j\,d\Omega$ are divergence/pressure gradient matrix and $J=(J_1,J_2)$ and $K=\int\left\{\frac{\partial\psi_{ki}}{\partial x}\frac{\partial\psi_{kj}}{\partial x}+\frac{\partial\psi_{ki}}{\partial y}\frac{\partial\psi_{kj}}{\partial y}\right\}d\Omega$ is a pressure stiffness matrix, where † is transpose of a matrix. $V^n, V^*, V^{n+1}$ are nodal vectors of velocity field, the pressure $p^n, p^{n+1}$, and the time interval $\Delta t$ is $(t_n, t_{n+1})$.

### 3.6 *Stream Function*

The understanding of flow structures is an essential component of fluid dynamics analysis. In a two-dimensional coordinate system, stream functions can be used to calculate flow structure, providing valuable quantitative insights. For each dimensional face of a three-dimensional coordinate system, multiple stream functions are required. Stream functions serve as powerful tools for illustrating flow structure, conveying important physical meaning, and facilitating mathematical analysis. Streamlines are used to interpret solid boundaries of a flow by representing its flow field in relation to local velocity vectors. They are useful for assessing recirculation regions quantitatively. The generation of stream functions becomes essential when simulating fluid flow problems using primitive variables. Using this technique to visualize the flow pattern in a clear and concise manner. The stream function must be understood prior to drawing streamlines from one node position to another. A family of curves that traverse the flow structure and can be calculated from the velocity gradient can describe the stream function. The variation of fluid particles along a single streamline or path line within a steady-state flow field remains constant. The stream function complies with Poisson's equation in Cartesian and cylindrical polar coordinates systems. In the case of incompressible two-dimensional flow, an appropriate vector potential, denoted as '$\Psi$,' as follows:

$$V=\nabla\times\Psi \quad (47)$$

Where,$\Psi=\{0,0,\Psi\}$ represents the stream function.

Since Cartesian coordinates in computation are a subclass of axisymmetric frames of reference, Assume the components of velocity are in the axial and radial directions of an axisymmetric cylindrical polar coordinate system ($r$,$z$). Stream function $\Psi(r,z)$ and velocity components fulfil the following relationships [5].

$$\frac{1}{r}\frac{\partial \Psi}{\partial r} = -v_z and \frac{1}{r}\frac{\partial \Psi}{\partial z} = v_r \quad (48)$$

For calculation purpose utilizing pseudo time stepping process, aforementioned (48) offers the resulting approach:

$$\frac{\partial \Psi}{\partial t} = \left(\frac{\partial^2 \Psi}{\partial r^2} + \frac{\partial^2 \Psi}{\partial z^2}\right) - r\frac{\partial v_z}{\partial r} - v_z + r\frac{\partial v_r}{\partial z} \quad (49)$$

After dividing by r gives Eq. (49) becomes:

$$\frac{1}{r}\frac{\partial \Psi}{\partial t} = \frac{1}{r}(\nabla^2 \Psi) - \frac{\partial v_z}{\partial r} - \frac{v_z}{r} + \frac{\partial v_r}{\partial z} \quad (50)$$

For time derivative Eq. (50) using forward time stepping approach along $(\Delta t)$ step, difference configuration of Eq. (50) develops:

$$\frac{1}{r}\left(\frac{\Psi^{n+1} - \Psi^n}{\Delta t}\right) = \frac{1}{r}(\nabla^2 \Psi^n) - \frac{\partial v_z}{\partial r} - \frac{v_z}{r} + \frac{\partial v_r}{\partial z} \quad (51)$$

Utilizing weighted residual technique, weak form of Eq. (51) turns into:

$$\frac{1}{\Delta t}\int_\Omega \frac{w}{r}(\Psi^{n+1} - \Psi^n)\, r d\Omega = \int_\Omega \frac{w}{r}(\nabla^2 \Psi^n)\, r d\Omega - \int_\Omega w\frac{\partial v_z}{\partial r} r d\Omega - \int_\Omega w\frac{v_z}{r} r d\Omega + \int_\Omega w\frac{\partial v_r}{\partial z} r d\Omega \quad (52)$$

A finite element approximation will be:

$$(\Psi, v_r, v_z) = \sum_{i=1}^{N}\left(\Psi_j, V_r^j, V_z^j\right)\Phi_i(r, z) \quad (53)$$

here, $\Phi_j$ is the quadratic basis function on nodal point $j$, and stream function'$\Psi_j$'. The radial and axial velocity elements are characterised by $\left(V_r^j, V_z^j\right)$ in $r$ and $z$directions separately.

Implementing finite element Galerkin approximation, where the weight function $(w_i)$ is taken correspondent to shape function $(\Phi_i)$ is demonstrated as follows [5]:

$$\sum_{i=1}^{N} w_i(x) = \sum_{i=1}^{N} \Phi_i\,(x) \quad (54)$$

Gives:

$$\frac{1}{\Delta t}\int_\Omega \Phi_i\Phi_j d\Omega \Delta\Psi_j^{n+1} = \int_\Omega \Phi_i\left(\nabla^2 \Phi_j\right) d\Omega \Psi_j^n - \int_\Omega \Phi_i \frac{\partial \varphi_j}{\partial r} r d\Omega\, v_z^j - \int_\Omega \Phi_i\Phi_j\, d\Omega v_z^j + \int_\Omega \Phi_i \frac{\partial \Phi_j}{\partial z} r d\Omega\, v_r^j \quad (55)$$

Green's theorem is applied to take integration, and ignoring the boundary integrals by insisting Dirichlet boundary conditions, can be expressed as:

$$\frac{1}{\Delta t}\int_\Omega \Phi_i\Phi_j d\Omega \Delta\Psi_j^{n+1} = -\int_\Omega \frac{\partial \Phi_i}{\partial r}\frac{\partial \Phi_j}{\partial r} + \frac{\partial \Phi_i}{\partial z}\frac{\partial \Phi_j}{\partial z} d\Omega \Psi_j^n - \int_\Omega \Phi_i \frac{\partial \Phi_j}{\partial r} r d\Omega\, v_z^j - \int_\Omega \Phi_i\Phi_j\, d\Omega v_z^j + \int_\Omega \Phi_i \frac{\partial \Phi_j}{\partial z} r d\Omega\, v_r^j \quad (56)$$

The Eq. (56) is shown in semi-implicit and explicit forms take on matrix-vector representation as:

$$\frac{1}{\Delta t} M\Delta\Psi_j^{n+1} = -S\Psi_j^n - D_1 v_z^j - M v_z^j + D_2 v_r^j \quad (57)$$

$$\left(\frac{1}{\Delta t}M + \frac{S}{2}\right)\Delta\Psi_j^{n+1} = -S\Psi_j^n - D_1 v_z^j - M v_z^j + D_2 v_r^j \quad (58)$$

Where, $M$ is mass like matrix with entries $\int_\Omega \Phi_i\Phi_j d\Omega$ and $S$ is identified as diffusion like term in matrix with entries:

$$\int_\Omega \frac{\partial \Phi_i}{\partial r}\frac{\partial \Phi_j}{\partial r} + \frac{\partial \Phi_i}{\partial z}\frac{\partial \Phi_j}{\partial z} d\Omega$$

In Eq. (57) and Eq. (58), $D_1$and $D_2$ are denoted as velocity gradient matrices with entries:

$\int \Phi_i \frac{\partial \Phi_j}{\partial r} r d\Omega$ and $\int \Phi_i \frac{\partial \Phi_j}{\partial z} r d\Omega$.

## 4. Results and Discussion

Newtonian fluids exhibit properties such as strain rate and shear-rate independence, resulting in linear shear viscosity, trivial stress difference, and a coherent viscosity. The published study provides intriguing insights into the behavior of rheological complex fluids when flowing through various porous media. Considering these facts, simulations have been conducted using an extended code developed specifically for this study. This code has already been expanded to incorporate parameters relevant to the investigation of channel flows through non-porous media. The simulations focus on Newtonian fluid flows in a conduit with a permeable material, and the findings are expressed in the streamline's configuration. The geometries considered include unidirectional and reversed flows both, and the different divisions are illustrated in Fig. 1. This study investigates the impact of porosity, with varying permeability values ranging from 0.1 to 0.00001, on inertia and pressure, allowing for monitoring and analysis of its effects.

### 4.1 *Mixing and Separating of Newtonian Fluid Flows in a Channel Filled with Porous Media ($G_1$)*

The specific problem involving combined mixing and separating flows is depicted in Fig. 1 (a). Numerical solutions are provided for various flow rates and flow directions, achieved by raising the Reynolds number. The focus of the investigation lies in understanding the influence of inertia, vortex size, and vortex intensity when a porous material fills the channel. Comparisons will be made between the effects of inertia and changes in pressure difference observed in channels without porous media, as well as findings from existing literature. Furthermore, the influence of permeability and porosity on the flow pattern will be thoroughly analyzed and conferred.

*4.1.1 Equal (1, 1) flow rate*

In this study, we analyze the influences of rising Reynolds number ranging from Re= 1 to 10000 on proportional flow rates, as illustrated in Fig. 2. It is essential to identify and comprehend new characteristics that arise because of changes in flow rates and conditions. Specifically, the objective is to evaluate the algorithm's performance and its ability to accurately replicate flow dynamics, particularly when adverse implications of flow inertia and flow rates interact in the conduit. For both reverse and unidirectional flows, simulation is initiated with $Re = 1$ to assess the stability of the program and its ability to simulate the existence of a space in the central axis and subsequent breakup. In the upper and lower exit portions of the geometry, this step is critical for capturing reversing and mixing zones. Simulations are conducted upto $Re = 10000$, starts from $Re = 1$. Up to $Re = 4000$, there is no evidence of vortex activity. When Reynolds number $Re = 5000$ is applied, there is a very weak vortex activity near the lower and upper nip of the insert plate towards exit flow. In Fig. 2, the vortex at the nip of the middle plate vanishes as the Reynolds number increases (at $Re = 6000\ and\ 10000$). Therefore, under low Reynolds numbers, there is no significant development of strong vortex behavior, indicating minimal opposing inertia effects on the flow structure, in accordance with previous literature [12]. It is further observed that the macroscopic local inertial term does not have any significant effect on the hydrodynamic pattern of the linear fluids in permeable medium. Based on the simulation findings, similar findings have been reported in the literature. Consequently, porous medium fields with least Darcy no: gain a negligible momentary time for all microscopic numbers. Results of this study indicate that local inertia can be disregarded, as its effects are insignificant within porous domains.

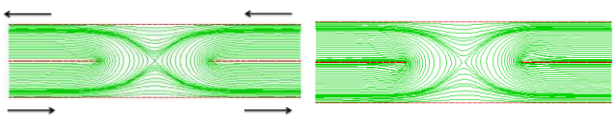

$Re = 1$ $Re = 3000$

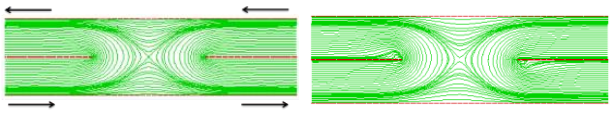

$Re = 4000$ $Re = 5000$

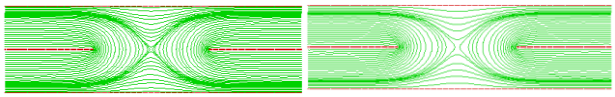

$Re = 600$ $Re = 10000$

**Fig. 2.** Mutual Mixing-Separating Contours for Newtonian Fluids Flowing In A Conduit With Porous Medium At Equal $(1, 1)$ Flow Rates, With Growing Re Ascending From Upper To Lower At Fixed Darcy's Number ($Da = 0.1$)

*4.1.2 Unequal (1, 1.5) flow rate*

The findings presented in Fig. 3 are based on numerical simulations for a conduit with porous medium, considering unequal flow rates of 1 and 1.5. The Reynolds number is increased from 1 to 10000 in these simulations to explore a variety of stream configurations. This study examines a setup that has two parallel streams with different stream rates in the top and bottom channels. Flow rate imbalance occurs between the top and bottom channel arms at a Reynolds number of 1 and unequal flow rates (1, 1.5). Consequently, flow descends from the top channel arm into the lower channel, resulting in an eddy forming along the lower channel wall within the central axis of the geometry. When the Reynolds number reaches 2000, observations indicate that an early response occurs in the departing flow of the bottom conduit arm, in which a feeble vortex develops close the verge of the centrally located insert plate. The vortex gradually grows in size and reaches stability at a Reynolds number of 3000. According to this early response, the relative flows exert an influence on the opposing inertia of the flow structure. The effects of inertia diminish with increasing Reynolds numbers, although an eddy remains on the lower channel wall throughout the test. In contrast with a channel without porous media, the existence of porous substances in the computational area does not significantly affect the inertia of Newtonian fluid flows. Because of the higher flow rate in the top conduit arm, the fluid is forced into the bottom conduit arm, resulting in a reversed flow toward both exits of the computational domain. As a result, vortices are witnessed on either segment of the centrally sited plate, specifically lower conduit arm near the exit.

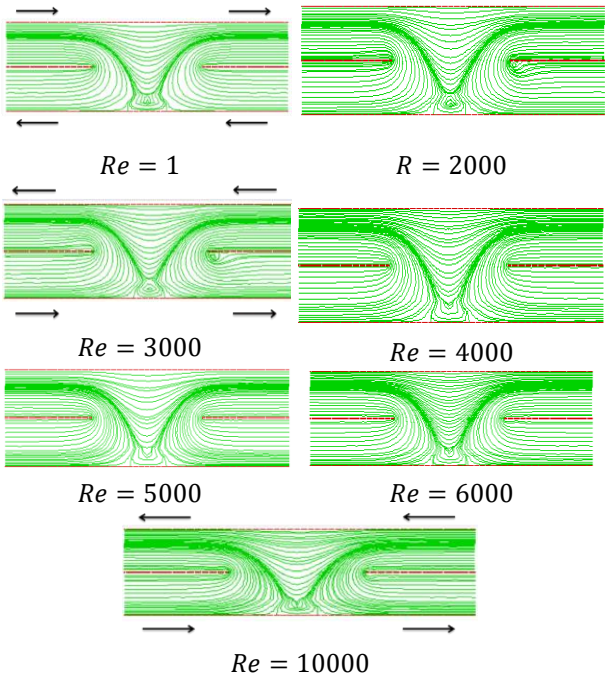


**Fig. 3.** In A Passage Fulfilled with Permeable Medium, The Stream Rate Of Newtonian Fluids Is Unequal (1, 1.5).

4.1.3 *Unequal (1, 2) flow rate*

Fig. 4 illustrates simulations of Newtonian fluid moving in a conduit with a permeable medium. Simulations are conducted with uneven flow rates in both arms of the channel (1, 2). The results of these simulations are similar to those of the previous work, and they are expressed in terms of streamlines across a choice of Reynolds numbers from 1 to 100,000. A Reynolds number of 1 lead to the flow in the minimal arm of the conduit pushing toward the middle gap and exiting, only touching the wall before returning to the upper arm without forming an eddy, contrary to a Reynolds number of 1.5. In the absence of an insert plate positioned centrally, vortices are evident behind one side. The vortices are located at the peak of the middle plate, aligned with the direction of the exit flow. According to Fig. 4, at a low Reynolds number of $Re = 2000$, the vortices in the bottom channel are located near the wall. As the Reynolds number rises, the vortices become inclined with the wall and exhibit increased stability (Fig. 4, $Re = 3000, 4000, and\ 5000$). When flow rates are unequal (1, 1.5), vortices are witnessed only at the insert plate of the bottom arm of the exit flow conduit. On the other side of the geometry, the upper conduit arm closes the insert plate showing no signs of vortex production. Considering the fluid parameters, it is evident that varying flow rates affect the opposing inertia of the flow structure. Overall, the simulations indicate that vortex activity is relatively low in porous channels with Newtonian fluids. Fluids mix in the central space of the domain and at the corners of the conduit as they approach the exit.

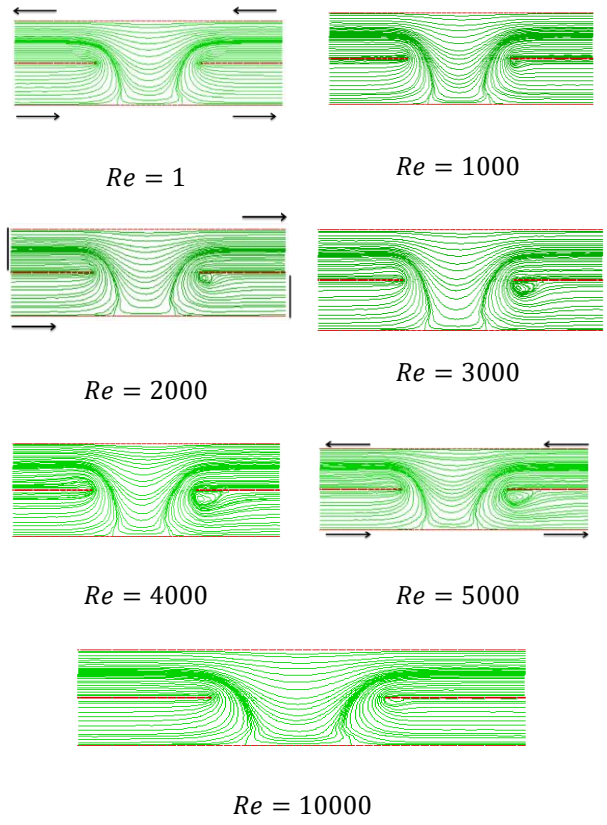


**Fig. 4.** The Mixing and Separation Of Newtonian Fluids In Porous Media Channels With Unequal Stream Rates (1, 2) Has Been Simplified

*4.2 Mixing and Separating of Newtonian Fluid Flows in A Channel Through Porous Media ($G_2$)*

A flow of Newtonian fluids within a single channel where the flow directions change is illustrated in Fig. 1 (b). Each arm of the channel has two inlets on the left side, and the lower arm has a single outlet on the right side. Changes in flow directions, increasing Reynolds numbers, and the inclusion of the Darcy term in momentum equations will be discussed here.

*4.2.1 Equal (1, 1) flow rate*

Fig. 5 illustrates the impact of growing Reynolds number between 1 and 1,000 and maintaining equal flow rates between (1, 1). To evaluate the algorithm's ability to reproduce flow behavior accurately, new characteristics resulting from variations in flow rates and directions are identified. In particular, the study aims to identify any significant changes in flow pattern caused by conflicting impacts of flow inertia. The disparate inertia has not produced any notable effects so far, even when Reynolds numbers reach 10000. Darcy's term, which mitigates the effect of disparate inertia on the flow pattern, can be credited

with this observation. It is important to note that the fluids mix within the bottom arm, moving in the direction of the exit point.

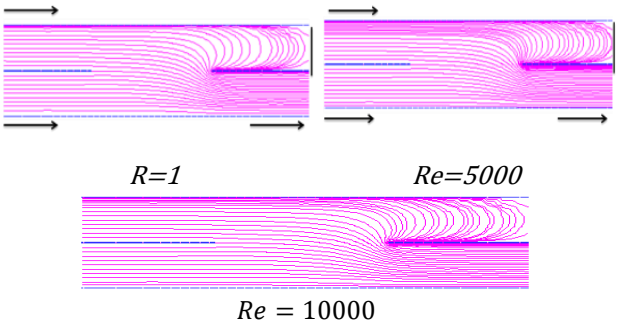


**Fig. 5.** Rationalise Function for Unidirectional Newtonian Fluid Streams Through A Porous Medium At The Same Flow Rate (1, 1)

*4.2.2 Unequal (1, 1.5) flow rate*

The outcomes of numerical simulations for Newtonian materials flowing through porous media with uneven flow rates (1, 1.5) are presented in Fig. 6. Various flow divisions were simulated by gradually increasing the Reynolds numbers ranging from 1 to 10000 for various flow partitions. In this configuration, there are two parallel flows in the top and bottom conduit arms, both moving in the similar direction in the direction of the alike exit in the lower conduit arm on the right. As a result of an increase in flow rate in the upper channel arm, there is a slight push towards the exit in the lower arm. The flow is pushed slightly towards the lower channel arm's exit corner as Re increases up to 10000. It remains unclear whether there are any other inertia-related effects when compared to the inertia-related effects of nonporous media under similar conditions. Because of the unidirectional nature of the flows in the lower conduit arm, the fluid flows mix towards the exit as Re increases. Despite this, even as Re reaches 10000, no signs of vortex are observed. Flow goes in the upper arm's silent zone from its right side, but no vortices are observed.

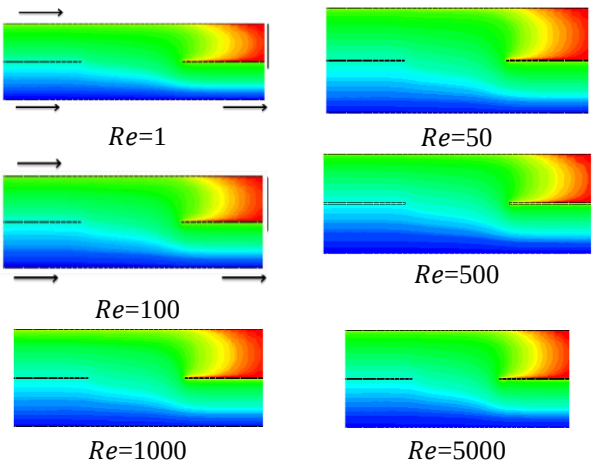


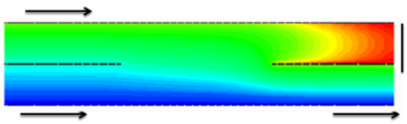

Re=10000

**Fig. 6.** Unidirectional Newtonian Fluid Streams Through a Permeable Medium with Unequal (1, 1.5) Stream Rates

*4.2.3 Unequal (1, 2) flow rate*

Numerical outcomes of Newtonian Fluid flow in a conduit full of a porous medium are shown in Fig. 7, illustrating uneven (1, 2) flow rates in both arms. The simulations cover a range of rising Reynolds numbers from 1 to 10000 for a variety of flow partitions. Flow toward the exit in the lower arm exhibits a slight increase in flow, but there is no significant opposing inertia. The top channel arm has a higher flow rate than the uneven (1, 1.5) or even equal (1, 1) flow rates in the bottom channel arm. When the Reynolds number (Re) increases to 10000, the lower channel arm's exit corner is slightly pushed towards the wall. In contrast to a conduit full of non-porous medium under the same settings, the flow rate or fluid properties change do not produce any other effects. The unidirectional nature of flow of fluid causes mixing in the lower channel arm as it approaches its exit. Due to the fact that there are no significant changes in the flow pattern within the field, fewer outcomes are presented in Fig. 8 than in the other two flow rates. The flow rates are illustrated in Fig. [5 to 6] which illustrate a conduit full of Newtonian materials through permeable medium.

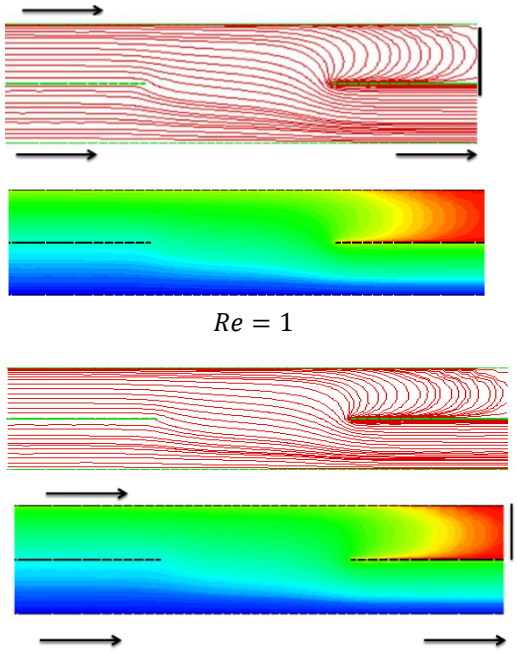


**Fig.7.** Unidirectional Newtonian Fluid Streams In A Channel Through A Permeable Medium With Unequal (1, 2) Stream Rates

*4.2.4 Effects of change in flow rate*

According to Fig. [5 to 7], the flow domain remains unchanged in all three sections, namely the bottom conduit arm, the upper conduit arm, and the separation gap in the middle. Fluid flow in the lower arm of the channel is gently predisposed by the change in flow rate in the upper arm of the channel, which causes it to flow in the direction of the fluid's exit. Due to the unidirectional flow, mixing occurs only in the downstream lower arm of the channel. The increase in Re (Reynolds number) does not result in any vortices at any of the three flow rates. Inertia was witnessed in the reversed flow instance mentioned earlier, but there were no significant changes in the unidirectional case.

*4.3 Mixing and Separating Newtonian Fluids Through Porous Media ($G_3$)*

Flows that combine mixing and separating are illustrated in Fig. 1 (c). The purpose of current investigation is to inspect the flow of Newtonian fluids within a conduit occupied with a porous medium with a particular focus on the variation in Reynolds number. Two opposing inlets are present in the flow configuration: one from the bottom arm on the left and other to the top arm on the right. On the right side of the lower arm, there is a single outlet. By altering flow rates in the top arm of the conduit, we examine inertia effects, pressure difference changes, and Darcy's number.

*4.3.1 Equal (1, 1) flow rate*

The research findings regarding the impact of rising Reynolds number ($1 \leq Re \leq 5000$) on the corresponding flow rates of linear fluids in a conduit occupied with porous medium are depicted in Fig. 8. Throughout the investigation, the Reynolds number was varied up to a maximum value of 5000. At a Reynolds number of 1, the flow motion in the channel starts from the lower arms and moves towards the upper arms. This flow pattern leads to flow reversal and stops fluid mixing in the central space of the domain.

Reynolds number up to 2000, no significant vortice development is observed, except for a displacement of the flow in the upper arm. However, as the Reynolds number is further increased, specifically at $Re = 3000$, a feeble vortex near the peck of a plate on the right side of the upper arm becomes noticeable. Additionally, some recirculation is observed in the right central axis of the plate on below of the bottom conduit arm. As the Reynolds number reaches 4000, the deceleration of vortices closes the middle axis of the plate on the right increases in dimension. It regulates location within the plate. The lesser swirls conserve its locations at an angle to the insert plates. They seem to turn into stable at Reynolds number of 5000, as illustrated in Fig. 8. The findings witnessed no intense vortex formation behavior at low Reynolds numbers. This aligns with the expected and previously reported weak differing inertia properties on the flow pattern, as discussed in the paper [12]. The observations reveal the occurrence of both unidirectional and reversed flows, with somewhat greater twisting observed in the reversed flow owing to the fluid flow's movement in the upper arm's prominent region and in the core void up to the peak of the duct arm's wall. The fluid exhibits increased mixing in the lower conduit arm, particularly in the segment on the way to flow partings.

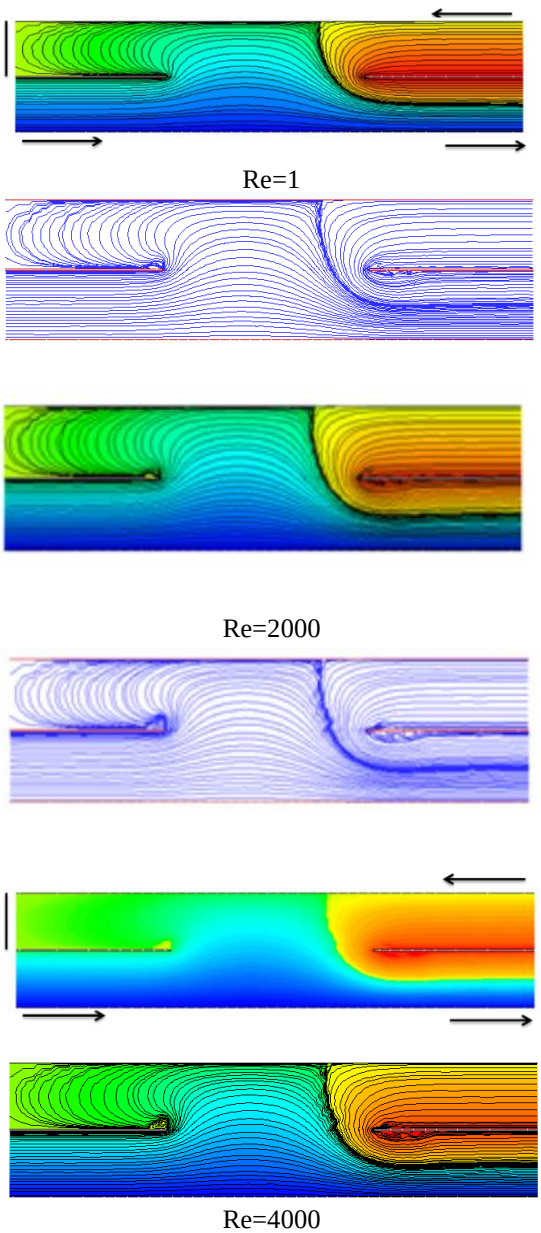

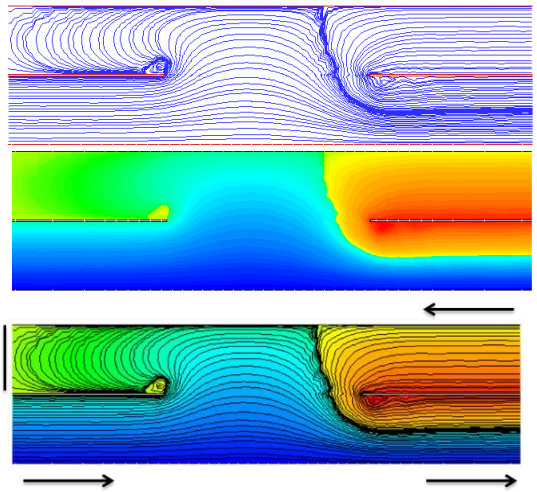

Re=5000

**Fig.8** An Equal $(1, 1)$ Stream Rate Newtonian Fluid Stream in A Permeable Passage Can Be Mixed and Separated By Means Of This Function

*4.3.2 Unequal (1, 1.5) flow rate*

The approximate outcomes illustrate the flow behavior of Newtonian fluids with unequal flow rates (1, 1.5) in two arms of a conduit occupied with porous media. The results of this study are illustrated in Fig. 9. Simulations were conducted by gradually increasing the Reynolds numbers $(1 \leq Re \leq 5000)$. In the lower arm toward the flow exit, a recirculation phenomenon was observed at Reynolds number Re = 2000 near the centrally positioned plate. A weak vortex was observed at the tip of the centrally located plate when equal flow rates (1, 1) were considered at $Re = 2000$. The vortex diminished, however, as the flow rate increased. Fig. [8 and 9] illustrate the impact of increased flow rate in the top conduit arm in comparison to the subordinate case. A vortex was observed near one side of the centrally located insert plates in the departure flow of the bottom conduit arm at Re = 3000. The vortex increased in size and adjusted its position within the plate as it grew. The top channel arm of $Re = 4000$ also showed a weak vortex lying flat on the insert plate, which lay near the centrally positioned insert plate. The vortices near the edges of the plates adjusted their positions and reached a steady state when $Re = 5000$ was reached. In the top channel arm, varying the flow rate significantly influenced the development of a vortex at the verge of the axis of plate, specifically from its left side. Fig. 8 illustrates how this vortex reappear at $Re = 4000$ as a result of an increase in Reynolds number. Equal flow rates produced the same mixing and separating effects. According to the above descriptions, both unidirectional and reversed flows exhibited similar behavior.

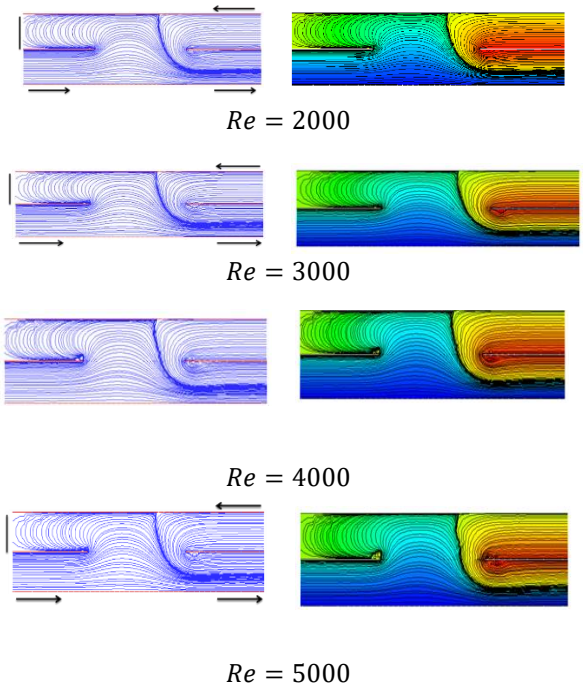


**Fig.9.** Optimize Mixing and Separating Newtonian Fluid Streams in A Passage Satiated With Permeable Media, Rising $Re$ From Top To Bottom, In Existence Of Unequal (1, 1.5) Stream Rates

*4.3.3 Unequal (1, 2) flow rate*

A simulation of linear fluid moves in a conduit occupied with a permeable medium is illustrated in Fig. 10 under uneven flow rates (1, 2) in each arm of the channel. Because of observations made in different sections of the flow domain, the following conclusions have been shown: The growth of vortices has not been observed in any section of the flow domain up to Reynolds number $(Re)$ 1000. An emerging vortex of smaller size emerges at $Re = 2000$ in the bottom channel arm of the central axis of the plate, immovable from the right. With the presence of the plate, the size of this vortex increases as Re reaches 3000. A second vortex forms at $Re = 4000$, on the right side of the central fixed plate, in the top arm, in the direction of the striking place of the field. In the presence of $Re = 5000$, vortices emerge, however on right location vortex becomes prominent. Eventually it splits into smaller vortices and form a meandering pattern when it adheres to each side of the edge in the lower and upper regions. There is apparent inertial opposition between the intensity of this splitting and the formation of smaller vortices as Reynolds numbers increase, which becomes more pronounced as the Reynolds number increases. There is a noticeable impact on the development of vortices at the central edge of the top

channel arm when the flow rate is changed from unequal to equal (1, 1.5) in the top conduit arm. As described in Fig. 6, this effect recurs at Re = 4000. Mixing and separating properties are like those observed in cases where the flow rates are equal. The behavior of unidirectional and reversed flows is like that of equal flow rates. As illustrated in Fig. 10 at $Re = 5000$, when the flow rate in the top channel arm changes from unven (1, 1.5) to equal (1, 2), there is a greater influence of inertia than for other relevant flow rates. Overall, these observations provide insight into the flow behavior and the effects of unequal flow rates in a conduit occupied with a porous medium under various Reynolds numbers.

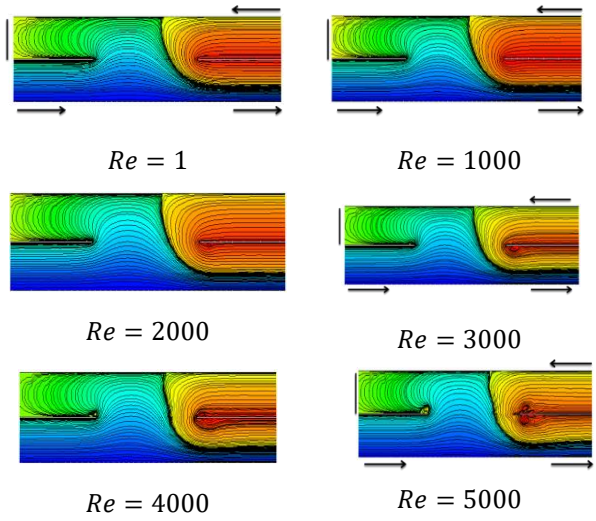


**Fig.10.** Streamline Combining and Splitting Newtonian Fluid Streaming in A Passage Fulfilled With Permeable Medium With Unequal Stream Rates (1, 2) As $Re$ Raises

*4.4.4 Flow rate changes and their effects*

A conduit occupied with porous media, specifically Newtonian fluid, is illustrated in Fig. 9 to 10 by examining streamline functions for unequal flows [(1, 1.5) and (1, 2)]. An increase in flow rates in one of the upper arms causes a vortex that has formed near the verge of the central fixed plate to disappear on the right sideways of the domain. The vortices become stronger and more intense in their formation for rising Reynolds number and the flow rate in the top arm is doubled. As a result of the observations, additional vortices can be observed to have spread, split, or even been generated. Increasing recirculation indicates greater influence of inertial effects near the sharp edge of the domain. Various Reynolds numbers and flow rates have been used to obtain solutions, but unidirectional flows were not achieved. It is more pronounced in the top channel arm as a result of the flow moving from the lower to upper arm in the prominent corner and middle separation gaps. The inverted flow obstructs the incoming flow from the upper conduit arm in the direction of the mid space, causing it to reverse direction and flow in the direction of the vent. Thus, mingling occurs primarily in the bottom conduit arm within the exit division.

*4.4.5 The impact of unidirectional flows and permeability on pressure*

A conduit occupied with porous media, where a Newtonian fluid is flowing, is illustrated by Fig. 11, which illustrates the impact of growing inertia and three corresponding flow rates on the difference of pressure. As the Reynolds number upsurges, the pressure difference in the conduit will fluctuate. As Reynolds numbers increase, as well as flow rates vary in the two arms of the conduit, the variable pressure intensifications almost linearly. During a change in flow rate, the permeability value is modified, resulting in an increase in pressure. As shown in Fig. 11, this change in permeability has a direct effect on the pressure difference. Consequently, a higher Reynolds number will result in a higher pressure, as can be witnessed in Fig. 11 during the relative flow rate comparison.

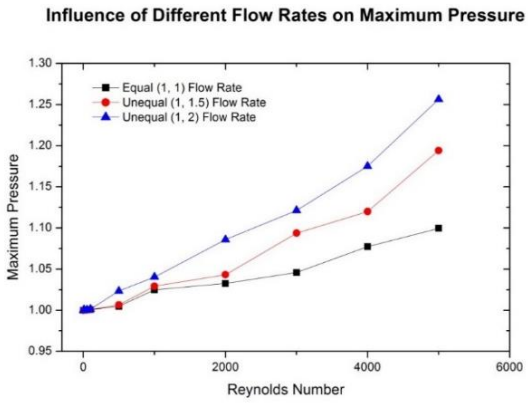


**Fig.11.** Analysis Of Extreme-Scrambled Pressure at Mixed Stream Rates in A Permeable Media Passage With Improving Inertia

*4.5 Newtonian Fluids Flow Unidirectional in a Porous Channel ($G_4$)*

Based on the unidirectional flow condition shown in Fig. 1(d), we will examine the development and intensity of a vortex, as well as the pressure difference. Our analysis focuses on a scenario where there is only one outlet on the right of the top arm of a conduit, and only one inlet on the left. This study

compares the results of permeability and porosity on flow rates, and flow directions in the three configurations mentioned earlier $(G_1, G_2 and G_3)$. The purpose of this research is to gain insight into how porosity and permeability influence vortex development intensity, and pressure difference in relation to different flow rates and directions observed in the configurations.

*4.5.1 Structure of flows affected by Inertia*

The simulations performed for unidirectional flows of linear liquids were conducted in a conduit occupied with porous media, as shown in following Fig. 12. Despite higher Reynolds numbers, specifically up to $Re = 100000$, no growth of vortices was observed. Additionally, when compared to reversed flow cases, inertial effects were found to have little influence on unidirectional flow. In terms of fluid flows in channels, the obtained results are consistent with findings reported in the existing literature [23].

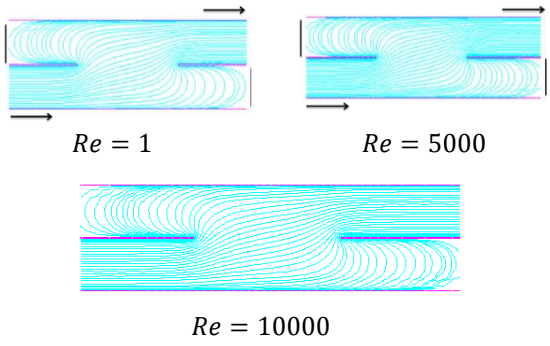


**Fig. 12.** Stream In a Passage Saturated with Permeable Media Consuming A Streamline Function

*4.5.2 Inertia and flow rate effects on pressure*

As the Reynolds number increases for Newtonian fluid flows, the difference pressure in the conduit through porous medium is shown in Fig. 13. The flow through two arms of the conduit, the variable pressure exhibits a nonlinear increase with increasing Reynolds number, resulting in varying pressures. According to Fig. 13, the permeability can be fixed at 0.001 for Reynolds numbers ranging from 1 to 5000. This results in a linear growth of the pressure difference within the Reynolds number range. As the permeability value decreases from $Re$ number $600\ to\ 10000$, the variable pressure rises, and the behavior becomes non-linear. Inertia as well as permeability are important factors affecting the pressure difference. The increase in pressure was initially minimal at lower Reynolds numbers and was not clearly visible on the graph. As a result, the vertical axis has been rescaled to better represent the data.

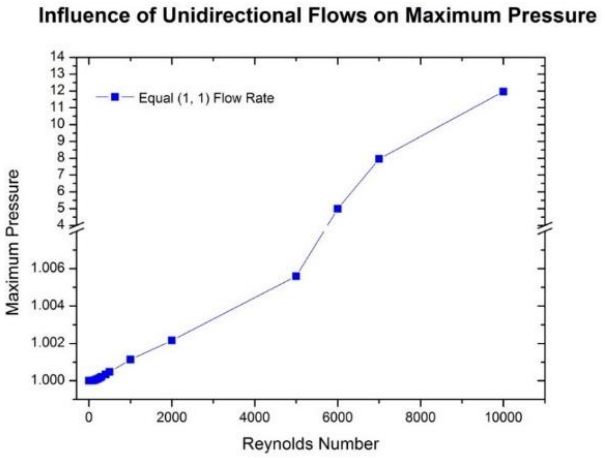


**Fig.13.** Extreme Pressure Scaled with Developing Inertia in A Passage Filled with Permeable Media in Unidirectional Newtonian Fluid Stream

## 5. Conclusion

Through numerical analysis, the effects of inertia on flow, pressure, and permeability were investigated in a pipe filled with essentially porous medium. The proposed algorithm was exposed to be stable and correct in predicting even and intricate streams, as well as bifurcations. The growth of vortex in a passage was found to decrease in the presence of porous materials. The rise of non-dimensional variable pressure was witnessed by the enhancement of the stream rate at the top arm of a conduit, and decreasing values of permeability had a similar influence on pressure. The analysis concludes that the stream behavior using power law index and the entire span of Darcy's and Forchheimer's numbers is little influenced by the inertial term.

## 6. References

[1] A. M. Afonso, M. A. Alves, R. J. Poole, P. J. Oliveira, and F. T. Pinho, “Viscoelastic flows in mixing-separating cells,” J. Eng. Math., vol. 71, pp. 3–13, 2011.

[2] S. O. S. Echendu, F. Belblidia, H. R. Tamaddon-Jahromi, and M. F. Webster, “Modelling with viscous and viscoplastic materials under combining and separating flow configurations,” Mech. Time-Dependent Mater., vol. 15, pp. 407–428, 2011.

[3] R. B. Khokhar, A. A. Bhutto, I. A. Bhutto, A. Mengal, F. Shaikh, and A. A. Shaikh, “Numerical analysis of non-newtonian fluid flows through an annulus occupied with or without porous materials,” Balochistan J. Eng. Appl. Sci., 2023.

[4] R. B. Khokhar, A. A. Bhutto, I. A. Bhutto, F. Sheikh, and M. A. Solangi, “Numerical analysis of newtonian fluids in channel flows using semi-implicit time stepping taylor-galerkin/pressure method,” Sci., vol. 4, no. 3, 2023.

[5] A. Baloch, P. Townsend, and M. F. Webster, “On the simulation of highly elastic complex flows,” J. Nonnewton. Fluid Mech., vol. 59, no. 2–3, pp. 111–128, 1995.

[6] R. B. Khokhar, “Numerical modelling of mixing and separating of fluid flows through porous media,” 2018.

[7] B. Xia and D.-W. Sun, “Applications of computational fluid dynamics (CFD) in the food industry: a review,” Comput. Electron. Agric., vol. 34, no. 1–3, pp. 5–24, 2002.

[8] R. B. Khokhar, A. A. Bhutto, N. F. Siddiqui, F. Shaikh, and I. A. Bhutto, “Numerical analysis of flow rates, porous media, and Reynolds numbers affecting the combining and separating of Newtonian fluid flows,” 2023.

[9] A. A. Bhutto, I. A. Bhutto, M. A. Soomro, U. A. K. Kashif, and I. A. Bhutto, “Numerical analysis of inertia effects on pressure and flow patterns in unidirectional and reversed newtonian fluid flows within a channel,” VFAST Trans. Math., vol. 11, no. 2, pp. 42–62, 2023.

[10] F. P. T. Baaijens, “Mixed finite element methods for viscoelastic flow analysis: a review,” J. Nonnewton. Fluid Mech., vol. 79, no. 2–3, pp. 361–385, Nov. 1998.

[11] M. A. Khaskheli, K. N. Memon, A. H. Sheikh, A. M. Siddiqui, and S. F. Shah, “Tank drainage for an electrically conducting newtonian fluid with the use of the bessel function,” Eng. Technol. Appl. Sci. Res., vol. 10, no. 2, pp. 5377–5381, 2020, doi: 10.48084/etasr.3322.

[12] K. N. Memon, M. K. Alam, J. Baili, Z. Nawaz, A. H. Shiekh, and H. Ahmad, “Analytical solution of tank drainage flow for electrically conducting Newtonian fluid,” Therm. Sci., vol. 25, no. Spec. issue 2, pp. 433–439, 2021, doi: 10.2298/TSCI21S2433M.

[13] M. Fortin and D. Esselaoui, “A finite element procedure for viscoelastic flows,” Int. J. Numer. Methods Fluids, vol. 7, no. 10, pp. 1035–1052, 1987.

[14] A. A. Bhutto, S. Memon, I. A. Bhutto, R. B. Khokhar, and A. A. Shaikh, “Numerical simulation of combustion chamber film cooling mechanism,” Balochistan J. Eng. Appl. Sci., 2023.

[15] I. A. Bhutto, I. Khan, M. Furqan, A. H. Alzahrani, A. A. Bhutto, and A. Singh, “Wall film cooling mechanism in liquid fuel combustion chamber containing gaseous hydrogen,” Int. J. Hydrogen Energy, vol. 52, pp. 246–255, 2024.

[16] A. A. Bhutto, M. Hussain, S. Feroz, A. Shah, and K. Harijan, “Computation of vortex driven flow instability through unsteady rans and scale resolving simulation,” Inst. Sp. Technol., vol. 12, no. 1, pp. 14–22, 2022.

[17] I. A. Bhutto, A. A. Bhutto, R. B. Khokhar, M. A. Soomro, and F. Shaikh, “The effect of uniform and exponential streams on Magnetohydrodynamic flows of viscous fluids.,” 2023.

[18] A. A. Bhutto, I. Ahmed, S. A. Rajput, and S. A. R. Shah, “The effect of oscillating streams on heat transfer in viscous magnetohydrodynamic MHD fluid flow,” 2023.

[19] T. Cochrane, K. Walters, and M. F. Webster, “Newtonian and non-Newtonian flow near a re-entrant corner,” J. Nonnewton. Fluid Mech., vol. 10, no. 1–2, pp. 95–114, 1982.

[20] A. A. Bhutto, S. F. Shah, R. B. Khokhar, K. Harijan, and M. Hussain, “to investigate obstacle configuration effect on vortex driven combustion instability,” 2023.

[21] A. A. Bhutto, K. Harijan, M. Hussain, S. F. Shah, and L. Kumar, “Numerical simulation of transient combustion and the acoustic environment of obstacle vortex-driven flow,” Energies, vol. 15, no. 16, p. 6079, 2022.

[22] B. Alazmi and K. Vafai, “Analysis of fluid flow and heat transfer interfacial conditions between a porous medium and a fluid layer,” Int. J. Heat Mass Transf., vol. 44, no. 9, pp. 1735–1749, 2001.

 

[23] M. A. Al-Nimr and T. K. Aldoss, “The effect of the macroscopic local inertial term on the non-Newtonian fluid flow in channels filled with porous medium,” Int. J. Heat Mass Transf., vol. 47, no. 1, pp. 125–133, 2004.

[24] K. Walters and M. F. Webster, “On dominating elastico-viscous response in some complex flows,” Philos. Trans. R. Soc. London. Ser. A, Math. Phys. Sci., vol. 308, no. 1502, pp. 199–218, 1982.

[25] T. Cochrane, K. Walters, and M. F. Webster, “On Newtonian and non-Newtonian flow in complex geometries,” Philos. Trans. R. Soc. London. Ser. A, Math. Phys. Sci., vol. 301, no. 1460, pp. 163–181, 1981.

[26] A. Afonso, M. A. Alves, R. J. Poole, P. J. Oliveira, and F. T. Pinho, “Viscoelastic low-Reynolds-number flows in mixing-separating cells,” Proceedings of the 6th International Conference on Engineering Computational Technology, 2008.

[27] K. U. Rehman, Q. M. Al-Mdallal, E.-S. M. Sherif, H. Junaedi, and Y.-P. Lv, “Numerical study of low Reynolds hybrid discretized convergent-divergent (CD) channel rooted with obstructions in left/right vicinity of CD throat,” Results Phys., vol. 24, p. 104141, 2021.

[28] S. A. R. Shah, K. N. Memon, S. F. Shah, A. H. Sheikh, and A. M. Siddiqui, “Delta perturbation method for thin film flow of a third grade fluid on a vertical moving belt,” Stat. Comput. Interdiscip. Res., vol. 4, no. 1, pp. 61–73, 2022.

[29] K. Dharejo, H. Shaikh, B. Shah, and A. Baloch, “Least square galerkin finite element study of newtonian fluids flow through channel with fixed rectangular single baffle,” Sindh Univ. Res. Journal-SURJ (Science Ser., vol. 50, no. 2, pp. 215–220, 2018.

[30] D. M. Hawken, H. R. Tamaddon-Jahromi, P. Townsend, and M. F. Webster, “A taylor–Galerkin-based algorithm for viscous incompressible flow,” Int. J. Numer. Methods Fluids, vol. 10, no. 3, pp. 327–351, 1990.

[31] F. T. Pinho and P. J. Oliveira, “Analysis of forced convection in pipes and channels with the simplified Phan-Thien–Tanner fluid,” Int. J. Heat Mass Transf., vol. 43, no. 13, pp. 2273–2287, 2000.

[32] R. I. Tanner, “Constitutive model for 7th workshop on numerical computations in viscoelastic flows,” 1989.

[33] H. Benzenine, R. Saim, S. Abboudi, and O. Imine, “Numerical simulation of the dynamic turbulent flow field through a channel provided with baffles: comparative study between two models of baffles: transverse plane and trapezoidal,” J. Renew. Energies, vol. 13, no. 4, pp. 639–651, 2010.

[34] J. Donea, “A Taylor–Galerkin method for convective transport problems,” Int. J. Numer. Methods Eng., vol. 20, no. 1, pp. 101–119, 1984.

[35] A. J. Chorin, “Numerical solution of the Navier-Stokes equations,” Math. Comput., vol. 22, no. 104, pp. 745–762, 1968.

[36] O. C. Zienkiewicz and R. Codina, “A general algorithm for compressible and incompressible flow—Part I. The split, characteristic-based scheme,” Int. J. Numer. methods fluids, vol. 20, no. 8-9, pp. 869–885, 1995.

[37] O. C. Zienkiewicz, R. L. Taylor, and R. L. Taylor, The finite element method: solid mechanics, vol. 2. Butterworth-heinemann, 2000.

[38] X.-D. Liu and P. D. Lax, “Positive schemes for solving multi-dimensional hyperbolic systems of conservation laws,” Sel. Pap. Vol. I, pp. 337–360, 2005.

[39] G. A. Sod, “A survey of several finite difference methods for systems of nonlinear hyperbolic conservation laws,” J. Comput. Phys., vol. 27, no. 1, pp. 1–31, 1978.

[40] E. O. Carew, P. Townsend, and M. F. Webster, “Taylor-Galerkin algorithms for viscoelastic flow: application to a model problem,” Numer. Methods Partial Differ. Equ., vol. 10, no. 2, pp. 171–190, 1994.

[41] J. Donea, “Recent advances in computational methods for steady and transient transport problems,” Nucl. Eng. Des., vol. 80, no. 2, pp. 141–162, 1984.

[42] M. A. Solangi, R. B. Khokhar, and A. Baloch, “A fem study for non-newtonian behavior of blood in plaque deposited capillaries: Analysis of blood flow structure,” Mehran Univ. Res. J. Eng. Technol., vol. 32, no. 2, pp. 277–282, 2013.

 

[43] J. Van Kan, “A second-order accurate pressure-correction scheme for viscous incompressible flow,” SIAM J. Sci. Stat. Comput., vol. 7, no. 3, pp. 870–891, 1986.

[44] J. Crank and P. Nicolson, “A practical method for numerical evaluation of solutions of partial differential equations of the heat-conduction type,” Adv. Comput. Math., vol. 6, no. 1, pp. 207–226, 1996.

[45] D. Solangi, H. Shaikh, R. B. Khokhar, and A. Baloch, “Numerical study of Newtonian blood flow through a plaque deposited artery,” Sindh Univ. Res. J. (Science Ser., vol. 45, no. 01, pp. 79–82, 2012.

 